# Optical Control of Field-Emission Sites by Femtosecond Laser Pulses

Hirofumi Yanagisawa,[1,*] Christian Hafner,[2] Patrick Doná,[1] Martin Klöckner,[1] Dominik Leuenberger,[1] Thomas Greber,[1] Matthias Hengsberger,[1] and Jürg Osterwalder[1]

[1]*Physik Institut, Universität Zürich, Winterthurerstrasse 190, CH-8057 Zürich, Switzerland*
[2]*Laboratory for Electromagnetic Fields and Microwave Electronics, ETH Zürich, Gloriastrasse 35, CH-8092 Zürich, Swizerland*

We have investigated field-emission patterns from a clean tungsten tip apex induced by femtosecond laser pulses. Strongly asymmetric modulations of the field-emission intensity distributions are observed depending on the polarization of the light and the laser incidence direction relative to the azimuthal orientation of tip apex. In effect, we have realized an ultrafast pulsed field-emission source with site selectivity. Simulations of local fields on the tip apex and of electron emission patterns based on photoexcited nonequilibrium electron distributions explain our observations quantitatively.

Applying strong electric fields to a metal enables field emission due to electron tunneling into the vacuum. Field emission from metallic tips with nanometer sharpness is particularly interesting due to the high brightness and coherence of the electron beams [1–6]. When a focused pulsed laser illuminates the tip, optical electric fields are enhanced at the tip apex (*local field enhancement*) due to the excitation of surface electromagnetic (EM) waves like, e.g., surface plasmon polaritons. Only recently, it was found that the enhanced fields induce pulsed field emission in combination with a moderate dc voltage applied to the tip [7–10]. Depending on the strength of the enhanced field, different field-emission processes become dominant [7]. For relatively weak fields, single electron excitations by single or multiphoton absorption are prevalent, and photoexcited electrons are tunneling through the surface potential barrier (*photo field emission*). On the other hand, very strong fields largely modify the tunneling barrier and prompt the field emission directly (*optical field emission*).

So far, the different emission processes were disputed in the literature, while the local field enhancement was treated as a static effect of the laser field such as the lightening rod effect [7,8,11,12]. However, dynamical effects are predicted to occur when the tip size is larger than approximately a quarter wavelength [13]. Here, we used a tip whose apex was approximately a quarter wavelength, and found that dynamical effects substantially influence the symmetries of field-emission intensity distributions. Varying the laser polarization changes these distributions substantially, an effect that had not been observed in earlier experiments [7,14]. At the same time, we have realized an ultrafast pulsed electron source with emission site selectivity of a few ten nanometers, improving thus on values reached in previous work based on polarization shaped laser pulses impinging on nanostructures [15]. Simulations of local fields on the tip apex and of electron emission patterns based on the photo field-emission model describe our observations quantitatively.

Figure 1 schematically illustrates our experimental setup. A tungsten tip with its axis along the (011) crystal direction is mounted inside a vacuum chamber ($3 \times 10^{-10}$ mbar). Laser pulses are generated in a Ti:sapphire oscillator (wavelength: 800 nm; repetition rate: 76 MHz; pulse width: 55 fs; average laser power $P_L$: 20 mW) and introduced into the vacuum chamber. The laser light was focused to 4 $\mu$m ($1/e^2$ radius) onto the tip apex. Linearly polarized laser light was used. The polarization vector can be changed within the transversal ($x$, $z$) plane by using a $\lambda/2$ plate. As shown in the inset, where the laser propagates towards the reader's eye as denoted by the circled dot, the polarization angle $\theta_P$ is defined by the angle between the tip axis and the polarization vector. The tip can be heated to clean the apex and also negatively biased for field emission. A position-sensitive detector in front of the tip measures the emission patterns. The spatial resolution of field-emission microscopy (FEM) is approximately
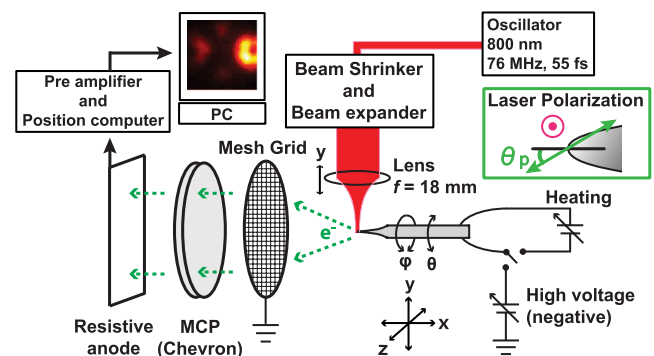


FIG. 1 (color online). Schematic diagram of the experimental setup. A tungsten tip is mounted inside a vacuum chamber. Laser pulses are generated outside the vacuum chamber. An aspherical lens is located just next to the tip to focus the laser onto the tip apex. Emitted electrons are detected by a position-sensitive detector in front of the tip. The polarization angle $\theta_P$ is defined in the inset, where the laser beam propagates towards the reader's eye (see text for further description).
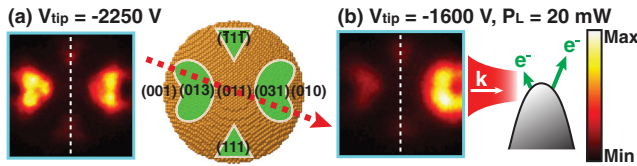
FIG. 2 (color online).   Electron emission patterns without laser (a), and with laser irradiation (b). $V_{\text{tip}}$ indicates the dc potential applied to the tip and $P_L$ indicates the laser power measured outside the vacuum chamber. The inset of (a) shows the front view of the atomic structure of a tip apex based on a ball model. The inset of (b) shows a schematic side view of the laser-induced field-emission geometry. A dashed white line denotes a mirror symmetry line of the atomic structure in each picture.

3 nm [1]. The tip holder can move along three linear axes $(x, y, z)$ and has two rotational axes for azimuthal $(\varphi,$ around the tip axis) and polar $(\theta,$ around the $z$ axis) angles. $\theta$ is set so that the tip axis is orthogonal to the laser propagation axis with a precision of $\pm 1°$, and the laser propagates parallel to the horizontal $y$ axis within an error of $\pm 1°$. In these experiments, the base line of the rectangular detector is approximately $20°$ off from the horizontal ($y$ axis) incidence direction, which means that the laser propagation axis is inclined by $20°$ from the horizontal line in the observed laser-induced FEM images [see dashed red arrow in Fig. 2(a)].

The field-emission pattern from the clean tungsten tip is shown in Fig. 2(a) where the most intense electron emission is observed around the (310)-type facets, and weaker emission from (111)-type facets. These regions are highlighted by green (gray) areas with white edges on the schematic front view of the tip apex in the inset of Fig. 2(a). The intensity map roughly represents a work function map of the tip apex: the lower the work function is, the more electrons are emitted. The relatively high work functions of (011)- and (001)-type facets [16] suppress the field emission from those regions.

The laser-induced FEM (LFEM) image in Fig. 2(b), taken with the light polarization oriented parallel to the tip axis $(\theta_P = 0)$, shows a striking difference in symmetry compared to that of the FEM image in Fig. 2(a). Emission sites are the same in both cases, but the emission pattern becomes strongly asymmetric with respect to the shadow (right) and exposed (left) sides relative to the laser incidence direction. The most intense emission is observed on the shadow side as illustrated in the inset of Fig. 2(b). Actually, the laser pulses arrive at an oblique angle as indicated by the dashed red arrow in the inset of Fig. 2(a), which slightly affects the symmetry with respect to the central horizontal line in the observed LFEM images (see below).

We found experimentally a strong dependence of the electron emission patterns on the laser polarization direction and azimuthal tip orientation. Figure 3 shows the LFEM patterns for different values of $\theta_P$ in $30°$ steps, and for four different azimuthal orientations $\varphi$ of the tip. The corresponding FEM images are also shown in the leftmost column. Throughout the whole image series, emission sites do not change, but intensities are strongly modulated resulting in highly asymmetric features.

When a laser pulse illuminates the metallic tip, surface EM waves [17] are excited, which propagate around the tip apex as illustrated schematically in Fig. 4(a). Because of the resulting interference pattern, the electric fields show an asymmetric distribution over the tip apex, depending also on the laser polarization. To simulate the propagation of these surface EM waves and the resulting field distributions, we used the software package MAX-1 for solving Maxwell equations based on the Multiple Multipole Program [19]. A dropletlike shape was employed as a model tip as shown in Fig. 4(b), with a radius of curvature of the tip apex of 100 nm, which is a typical value for a clean tungsten tip. The dielectric function $\epsilon$ of tungsten at 800 nm was used: a real part $\Re(\epsilon) = 5.2$ and an imaginary part $\Im(\epsilon) = 19.4$ [20]. By using different droplet sizes, it was verified that the model
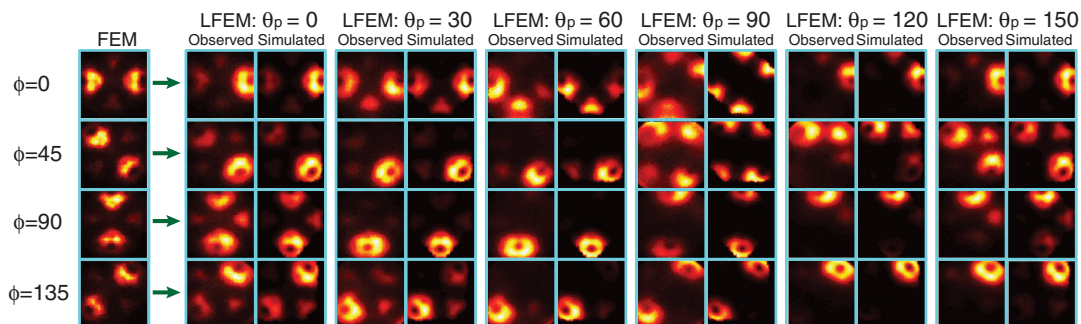


FIG. 3 (color online).   Comparison of measured and simulated laser-induced FEM (LFEM) images for different light polarization angles $\theta_P$ and for different azimuthal orientations $\varphi$ of the tip. The leftmost column gives the FEM images without laser irradiation for four different azimuthal angles ($V_{\text{tip}} = -2250$ V). For the same azimuthal angles, observed LFEM images are shown as a function of polarization angle $\theta_P$ in $30°$ steps ($V_{\text{tip}} \approx -1500$ V and $P_L = 20$ mW). The simulated LFEM images from the photo field-emission model, in which $V_{\text{tip}}$ and $P_L$ were set as in the corresponding experiments, are shown on the right-hand side of the observed LFEM images. The color scale and laser propagation direction are the same as in Fig. 2.

tip is long enough so as to mimic the infinite length of the real tip.

Figure 4(b) shows the calculated time-averaged field distribution over a cross section of the model tip, where the polarization vector has been chosen parallel to the tip axis ($\theta_P = 0°$). The laser propagates from left to right. The field distribution is clearly asymmetric with respect to the tip axis, with a maximum on the shadow side of the tip. This is consistent with our observations in Fig. 2(b) where the field emission is enhanced on the shadow side. Figure 4(c) shows, in a front view, time-averaged field distribution maps from the white dashed line region of the model tip in Fig. 4(b). This area corresponds roughly to the observed area in our experiments. The field distribution changes strongly depending on the polarization angle. Note that the positions of the maximum local fields are almost the same for wavelengths in the range between 750 and 850 nm; therefore, the simulation at the center frequency of the pulse alone (800 nm) is sufficient.

From the calculated local fields, we further simulated the LFEM images by considering the photo field-emission mechanism. The current density $j_{calc}$ of field emission can be described in the Fowler-Nordheim theory based on the free-electron model as follows [1,2,21,22],

$$j_{calc} = \frac{em}{2\pi^2\hbar^3} \int_{-W_a}^{\infty} \int_{-W_a}^{W=E} D(W, \Phi, F) f(E) dW dE. \quad (1)$$

Here, $e$ is the electron charge and $m$ the electron mass, $-W_a$ is the effective constant potential energy inside the metal, $W$ is the normal energy with respect to the surface, and $E$ is the total energy. Important factors are $D(W, \Phi, F)$, and $f(E)$. $D(W, \Phi, F)$ is the probability that an electron with the normal energy $W$ penetrates the surface barrier. It depends exponentially on the triangular-shaped potential barrier above $W$, as indicated in Fig. 4(d), which is deter-

mined by the work function $\Phi$ and the electric field $F$ just outside the surface. $f(E)$ is an electron distribution function. In the case of field emission, we have $F = F_{dc}$, where $F_{dc}$ is the applied dc electric field and $f(E)$ is the Fermi-Dirac distribution for an equilibrium state at a temperature of 300 K.

In the photo field-emission model, $F$ still equals $F_{dc}$, but the electron distribution is strongly modified by the electron-hole pair excitations due to single and multi-photon absorption, resulting in a nonequilibrium distribution characterized by a steplike profile, as illustrated in Figs. 4(d) [23,24]. For example, one-photon absorption creates a step of height $S_1$ from $E_F$ to $E_F + h\nu$ by exciting electrons from the region $E_F - h\nu$ to $E_F$. Absorption of a second photon creates a step of height $S_2$ from $E_F + h\nu$ to $E_F + 2h\nu$, where $S_2 = S_1^2$. We included absorption of up to four photons. The step height $S_1$ is proportional to the light intensity $I$. In the vicinity of the tip, we have $I \propto F_{laser}^2$ where $F_{laser}$ is the enhanced optical electric field that varies over the tip apex as illustrated in Fig. 4(c) [25].

There are three adjustable parameters in our calculations of $j_{calc}$: $\Phi$, $F$, and $S_1$. They are all functions of position on the tip apex. $\Phi$ and $F$ maps on the tip apex were obtained from the measured FEM images in the following way: a relative $F$ distribution was generated by MAX-1. We then obtained the $\Phi$ map by inserting $F$ into Eq. (1) and fitting $j_{calc}$ to the symmetrized experimental FEM current density $j_{exp}$. The resulting $\Phi$ map was compared to known values for several surface facets of tungsten, and the absolute values were adjusted by multiplying the $F$ distribution with a constant factor. Thus, a full $\Phi$ map and absolute values for $F$ were obtained. The resulting $\Phi$ values are approximately 4.9, 4.6, and 4.45 eV for (011), (001), and (310) surfaces, respectively, which are in fair agreement with known values [16,26]. A field strength $F$ of 2.15 V/nm results at the tip apex center for the FEM image taken with $V_{tip} = -2250$ V, which is a typical value for FEM. The LFEM experiments were carried out with a reduced tip voltage $V_{tip} \approx -1500$ V; hence, we used a scaled-down value of 1.43 V/nm in the LFEM simulations.

Substituting the obtained $\Phi$ and $F$ distribution maps into Eq. (1), and using a nonequilibrium electron distribution $f(E)$, the absolute values of $S_1$ over the tip apex were determined by fitting the measured total current from the (310) facet on the right-hand side of the LFEM image in Fig. 2(b). The resulting maximum value for $S_1$ was $1.6 \times 10^{-6}$. By substituting all the adjusted parameters into Eq. (1), we could simulate all the LFEM images. The calculated current densities on the tip apex were projected to the flat screen by following the static field lines. The simulated images can now be directly compared to the experimental images (Fig. 3): they are in excellent agreement in every detail. This comparison clearly demonstrates that the observed strongly asymmetric features originate from the modulation of the local photo fields. The two-
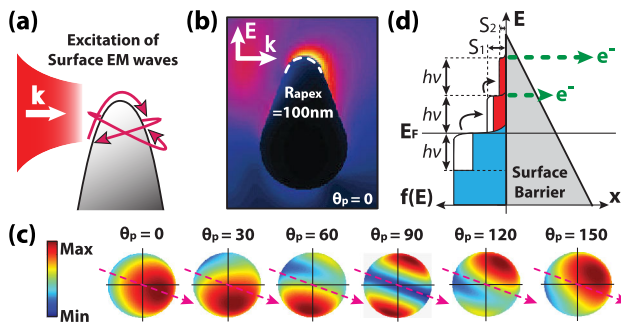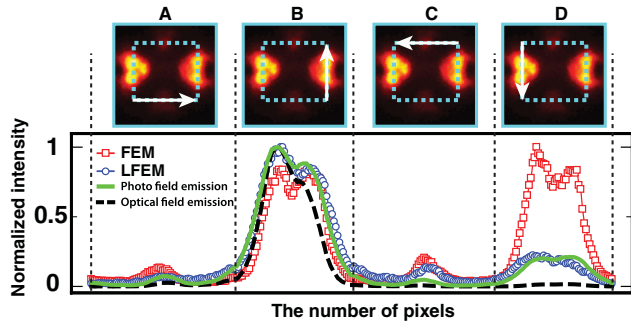


FIG. 4 (color online).   Schematic illustration of the excitation and interference of surface EM waves (a). The calculated time-averaged field distribution around the model tip is shown in a linear color scale in (b) for $\theta_P = 0°$. Highest field values are represented in yellow (brightest color). In (c), the time-averaged field distributions are given in a front view of the model tip for different polarization directions $\theta_P$. The laser propagation direction is indicated by dashed red arrows, it is the same as in the experiment. (d) shows a schematic diagram of photo field-emission from a nonequilibrium electron distribution.

FIG. 5 (color online). Line profiles extracted from the ob-
served FEM images (red line with squares), LFEM images
(blue line with circles), and from LFEM images simulated by
the photo field-emission model (green solid line) and the optical
field-emission model (black dashed line) at $[\varphi = 0°, \theta_P = 0°]$.
The whole scanned line corresponds to the unfolded rectangle
indicated by the dashed blue line in the FEM figures above, and
the corresponding sides are indicated by white arrows. Each line
profile has been normalized by the maximum value.

photon excitations strongly dominate the emission current
due to the thin barrier width [Fig. 4(d)], even though the
step height $S_2$ is very small. This is in line with the
observed laser power dependence of the integrated inten-
sities which shows a clearly nonlinear behavior.

Finally, we simulated the LFEM images also for the
optical field-emission process and compared the resulting
intensity distributions with those of the photo field-
emission model. In the optical field-emission model, the
Fermi-Dirac distribution is not modified, but instead, the
electric field $F$ in Eq. (1) is expressed as $F = F_{dc} + F_{laser}^{\perp}$
where $F_{laser}^{\perp}$ is the normal component of $F_{laser}$. The abso-
lute values for $F_{laser}^{\perp}$ on the tip apex were determined in the
same way as described above for the $S_1$ values. The result-
ing maximum value for $F_{laser}^{\perp}$ was 0.71 V/nm.

Figure 5 shows line profiles extracted from the observed
FEM and LFEM images, and from the corresponding
simulations for both photo field-emission and optical
field-emission models at $[\varphi = 0°, \theta_P = 0°]$, which were
all normalized by their maximum value. The whole
scanned line corresponds to the rectangle indicated in the
example FEM image. The measured LFEM profile clearly
shows the asymmetric feature as seen in the regions $B$ and
$D$. The photo field-emission model (green solid line)
catches this asymmetry much more quantitatively than
the optical field-emission model (black dashed line), as
can be best seen in region $D$. Therefore, the local fields in
our experiment are still weak enough such that the photo
field-emission process is the dominant one.

In summary, we have demonstrated the realization of an
ultrafast pulsed field-emission source with convenient con-
trol of nanometer sized emission sites by the laser polar-
ization and incident laser angle relative to the azimuthal
orientations. The photo field-emission model reproduces

our observations well. Maybe the most interesting appli-
cations will arise when two laser pulses with different
polarizations or paths are used. Electron emission from
two independent sources but originating from the same
quantum state could be studied [5,6]. This should create
new opportunities for addressing fundamental questions in
quantum mechanics such as anticorrelation of electron
waves in vacuum [27], or for new directions in electron
holography [28].

---

*hirofumi@physik.uzh.ch
 [1] R. Gomer, *Field Emission and Field Ionization* (American
     Institute of Physics, New York, 1993).
 [2] G. Fursey, *Field Emission in Vacuum Microelectronics*
     (Kluwer Academic/Plenum Publishers, New York, 2003).
 [3] H.-W. Fink, IBM J. Res. Dev. **30**, 460 (1986).
 [4] T.-Y. Fu *et al.*, Phys. Rev. B **64**, 113401 (2001).
 [5] B. Cho *et al.*, Phys. Rev. Lett. **92**, 246103 (2004).
 [6] C. Oshima *et al.*, Phys. Rev. Lett. **88**, 038301 (2002).
 [7] P. Hommelhoff *et al.*, Phys. Rev. Lett. **96**, 077401 (2006).
 [8] P. Hommelhoff *et al.*, Phys. Rev. Lett. **97**, 247402 (2006).
 [9] C. Ropers *et al.*, Phys. Rev. Lett. **98**, 043907 (2007).
[10] B. Barwick *et al.*, New J. Phys. **9**, 142 (2007).
[11] L. Novotny, J. Am. Ceram. Soc. **85**, 1057 (2002).
[12] B. Hecht and L. Novotny, *Principles of Nano-Optics*
     (Cambridge University Press, Cambridge, 2005).
[13] Y. C. Martin *et al.*, J. Appl. Phys. **89**, 5774 (2001).
[14] Y. Gao *et al.*, Phys. Rev. B **35**, 4284 (1987).
[15] M. Aeschlimann *et al.*, Nature (London) **446**, 301 (2007).
[16] C. Kittel, *Introduction to Solid State Physics* (John Wiley
     & Sons, New York, 2005), 8th ed.
[17] Surface EM waves are classified in terms of the dielectric
     functions of the material. If $\Re(\epsilon)$ is negative, then the
     surface EM waves are proper *surface plasmon polaritons*.
     If $\Re(\epsilon)$ is positive and $\Im(\epsilon)$ is large, the term *Zenneck
     waves* is more appropriate. Since they represent the same
     concept in the sense of EM waves coupling with the
     surface charges [18], we shall use the term *surface EM
     waves*.
[18] F. Yang *et al.*, Phys. Rev. B **44**, 5855 (1991).
[19] http://alphard.ethz.ch/.
[20] *CRC Handbook of Chemistry and Physics*, edited by D. R.
     Lide (CRC Press, Boca Raton, FL, 2009), 90th ed.
[21] E. L. Murphy *et al.*, Phys. Rev. **102**, 1464 (1956).
[22] R. D. Young, Phys. Rev. **113**, 110 (1959).
[23] L. Wu *et al.*, Phys. Rev. B **78**, 224112 (2008).
[24] M. Lisowski *et al.*, Appl. Phys. A **78**, 165 (2004).
[25] M. Merschdorf *et al.*, Phys. Rev. B **70**, 193401 (2004).
[26] C. E. Mendenhall *et al.*, Phys. Rev. **51**, 346 (1937).
[27] H. Klesel *et al.*, Nature (London) **418**, 392 (2002).
[28] A. Tonomura, Rev. Mod. Phys. **59**, 639 (1987).